New Journal of Physics
The open access journal at the forefront of physics

Deutsche Physikalische Gesellschaft DPG IOP Institute of Physics

PAPER • OPEN ACCESS

Generation of isolated soft x-ray attosecond pulses with mid-infrared driving lasers via transient phase-matching gating

To cite this article: Baochang Li *et al* 2021 *New J. Phys.* **23** 073051

New Journal of Physics
The open access journal at the forefront of physics

Deutsche Physikalische Gesellschaft DPG
IOP Institute of Physics

Published in partnership with: Deutsche Physikalische Gesellschaft and the Institute of Physics

OPEN ACCESS

RECEIVED
28 March 2021

REVISED
7 July 2021

ACCEPTED FOR PUBLICATION
12 July 2021

PUBLISHED
30 July 2021

PAPER

Generation of isolated soft x-ray attosecond pulses with mid-infrared driving lasers via transient phase-matching gating

Baochang Li[1], Kan Wang[1], Xiangyu Tang[1], Yanbo Chen[1], C D Lin[2] and Cheng Jin[1,*]

[1] Department of Applied Physics, Nanjing University of Science and Technology, Nanjing, Jiangsu 210094, People's Republic of China
[2] J. R. Macdonald Laboratory, Department of Physics, Kansas State University, Manhattan, Kansas 66506, United States of America
[*] Author to whom any correspondence should be addressed.

E-mail: cjin@njust.edu.cn

Keywords: isolated attosecond pulses, soft x-ray, high harmonic generation, mid-infrared, phase matching

Abstract

Isolated attosecond pulses (IAPs) in the soft x-ray (SXR) region are highly desirable for attosecond time-resolved experiments. Here we identify a transient phase matching gating method for the generation of such IAPs with mid-infrared (MIR) lasers. This gating method works when a loosely focused, long-duration MIR Gaussian driving beam is slightly reshaped during its propagation in the gas medium under the 'critical' ionization condition. Quantitatively, the calculated coherence length of high harmonic is used to analyze the mechanism of the gating method, by using one-dimensional plane-wave beams and by comparing 2000 nm and 800 nm lasers. The robustness of the generation method is checked by varying laser's carrier-envelope-phase and gas pressure. This gating method provides with an alternative route to efficiently produce tabletop ultrashort attosecond SXR light sources with the emerging MIR lasers.

1. Introduction

High harmonic generation (HHG) from the interaction of a focused infrared laser with a gaseous medium is a highly nonlinear process [1–3]. It provides a unique approach to generate coherent tabletop light sources with ultrashort duration and short wavelength from the extreme ultraviolet (XUV) to soft x-rays (SXRs) [4–6]. The generation of high harmonics can be understood by the three-step model [7, 8], in which harmonics are repeatedly emitted via tunelling ionization, electron propagation and recombination over every half optical cycle (o.c.) of the driving laser. The HHG thus generated appears temporally in the form of an attosecond pulse train (APT) [9]. To have a better temporal resolution, one would like an isolated attosecond pulse (IAP), which can be generated by a variety of gating schemes, mostly limiting the efficient HHG process to occur only once over a short period.

Since the first report of a 650 as IAP generation in 2001 [10], in the last two decades, several methods have been developed to produce IAPs in the XUV region based on the traditional Ti:sapphire lasers. These include amplitude gating [10, 11], ionization gating [12], polarization gating [13], double-optical gating [14, 15], attosecond lighthouse [16], multi-color waveform synthesis [17–20], phase-matching in the overdriven regime [21], and so on. With the advance of mid-infrared (MIR) laser technology [5, 22–24], HHG spectrum can be extended to higher photon energies because the cutoff energy of a single-atom harmonic emitter is proportional to λ_L^2, where λ_L is the laser wavelength. Consequently, IAPs in the SXR region have come into existence. Using the autocorrelation method, Chen *et al* [25] demonstrated the generation of IAP at photon energies up to 180 eV with 2 μm, multi-cycle laser pulses. The standard attosecond streaking method has also been implemented to measure the SXR IAP [26]. For example, Cousin *et al* [27] reported an IAP in the SXRs with duration of 322 as, driven by a sub-two-cycle, carrier-envelope-phase (CEP) stabilized 1.85 μm laser pulse. Li *et al* [28] reported a 53 as IAP with a bandwidth of 100–300 eV, with a two-cycle 1.8 μm laser. Similarly, Gaumnitz *et al* [29] claimed a 43 as

pulse with bandwidth of ∼100 eV was generated with a CEP-stable MIR (1.8 μm) laser. Additionally, several groups have employed MIR laser pulses to produce continuum SXR harmonic spectra but the temporal character was not determined. They have been identified as generation of continuous harmonic spectra up to the carbon K-edge of 284 eV, with the rotation of the driving laser's wavefront by Silva *et al* [30], the production of 0.5 keV supercontinuum spectra by Teichmann *et al* [31], the MIR-driven high harmonics with photon energies up to 600 eV in the overdriven regime by Johnson *et al* [32], the demonstration of high efficiency water-window HHG with TW class MIR laser under a loose focusing geometry by Fu *et al* [33], etc. As MIR lasers are becoming widely available in the laboratories, it is highly desirable to develop other gating methods for the generation of high-flux IAPs in the SXR regime.

The desirable gating method is to generate harmonics efficiently to ensure high SXR photon flux for attosecond time-resolved experiments. It has been established that single-atom harmonic yield drops quickly with the increase of the laser wavelength, commonly as [34, 35] $\lambda_{\mathrm{L}}^{-(4-6)}$, and inclusion of macroscopic propagation effects in the gaseous medium further enhances the decrease of the yield with laser wavelength [36, 37]. The 'critical' ionization is defined when the ionization-dependent phase mismatch caused by free electrons is balanced by neutral atom dispersion, which decreases with the ionization level [5, 38]. Blow the 'critical' ionization level, the unfavorable wavelength scaling of HHG yield can be compensated at good phase-matching conditions by increasing gas pressure. The phase-matched cutoff energy is scaled as [38] $\lambda_{\mathrm{L}}^{(1.6-1.7)}$. With the increase of laser wavelength, the 'critical' ionization level gradually decreases, and the required laser intensity is decreased as well [39, 40]. If the pulse energy of input laser is fixed, this would enable a loosely focused beam.

In this work, our main goal is to establish a transient phase-matching gating for efficient generation of SXR IAPs with MIR lasers. This method works when ionization is at the 'critical' level and the Gaussian beam is loosely focused [41]. This paper is structured as follows: section 2 introduces single-atom HHG theory, one- and three-dimensional propagation models for simulating macroscopic HHG in the gas medium, and theory for synthesizing attosecond pulses. Section 3 compares high harmonics and attosecond pulses driven by IR (800 nm) and MIR (2000 nm) lasers for a one-dimensional ideal beam and a three-dimensional (3D) Gaussian beam, and analyzes the transient phase-matching mechanism for generating IAP by calculating the coherence length of the harmonics. The conclusions are presented in section 4.

2. Theoretical methods

2.1. Single-atom response

In our numerical calculation, the single-atom harmonics are calculated using the quantitative rescattering (QRS) model [42–44]. The model is modified from the strong field approximation (SFA) [45] but it is nearly as accurate as solving the 3D time-dependent Schrödinger equation (TDSE) 'exactly'. The accuracy of single-atom HHG results from the QRS model has been established by comparing with those from solving 3D TDSE for single-color [46] or two-color laser pulses [47]. Within the QRS, the complex-valued induced dipole $D(\omega)$ of an atomic target can be written as

$$D(\omega) = W(\omega)\, d(\omega). \tag{1}$$

Here $d(\omega)$ is the complex photo-recombination transition dipole matrix element, and $W(\omega)$ is the complex microscopic electron wave packet. For the former, it can be accurately calculated through solving the time-independent Schrödinger equation including the Coulomb potential effect, and the latter can be calculated from the SFA. Computationally, the QRS model demands much less time than solving the 3D TDSE, with the computation time the same as SFA, thus making the calculation of macroscopic HHG efficiently.

2.2. Macroscopic propagation in the gas medium

To fully simulate SXR high harmonic radiation in a macroscopic gas medium, one needs to insert the single-atom response into the Maxwell's wave equations for the high-harmonic field. Meanwhile, the equation describing the evolution of the fundamental laser field is also solved, where effects of diffraction, nonlinear self-focusing, ionization, and medium dispersion are all included in the equation. The details of these equations have been presented in references [36, 48, 49] Here we only give some key equations.

We solve the propagation equations in a moving coordinate frame ($z' = z$ and $t' = t - z/c$). The 3D equations of the fundamental driving laser in the frequency domain can be written as

$$\nabla_{\perp}^{2}\tilde{E}_{\mathrm{f}}(r, z', \omega) - \frac{2i\omega}{c}\frac{\partial \tilde{E}_{\mathrm{f}}(r, z', \omega)}{\partial z'} = \tilde{G}(r, z', \omega), \tag{2}$$

and

$$\tilde{E}_{\mathrm{f}}\left(r,z',\omega\right)=\hat{F}\left[E_{\mathrm{f}}\left(r,z',t'\right)\right], \tag{3}$$

$$\tilde{G}\left(r,z',\omega\right)=\hat{F}\left\{\mu_0\frac{\partial J_{\mathrm{abs}}\left(r,z',t'\right)}{\partial t'}+\frac{\omega_{\mathrm{p}}^2}{c^2}E_{\mathrm{f}}\left(r,z',t'\right)-2\frac{\omega_0^2}{c^2}\left[\delta_1+\eta_2 I\left(r,z',t'\right)\right]E_{\mathrm{f}}\left(r,z',t'\right)\right\}. \tag{4}$$

Here $\hat{F}$ is the Fourier transform operator, $E_{\mathrm{f}}(r,z',t')$ is the transverse electric field of the driving laser. J_{abs}, δ_1, n_2, ω_{p} represent absorption caused by ionization, atomic dispersion, nonlinear Kerr coefficient, and plasma frequency, respectively.

The 3D propagation equations of high-harmonic field in the macroscopic medium are:

$$\nabla_{\perp}^2\tilde{E}_{\mathrm{h}}\left(r,z',\omega\right)-\frac{2i\omega}{c}\frac{\partial\tilde{E}_{\mathrm{h}}\left(r,z',\omega\right)}{\partial z'}=-\omega^2\mu_0\tilde{P}\left(r,z',\omega\right), \tag{5}$$

where

$$\tilde{E}_{\mathrm{h}}(r,z',\omega)=\hat{F}\left[E_{\mathrm{h}}\left(r,z',t'\right)\right], \tag{6}$$

$$\tilde{P}(r,z',\omega)=\hat{F}\left\{\left[n_0-n_{\mathrm{e}}\left(r,z',t'\right)\right]D\left(r,z',t'\right)-\frac{2}{\mu_0c^2}\left(\delta_{\mathrm{h}}+i\beta_{\mathrm{h}}\right)E_{\mathrm{h}}\left(r,z',t'\right)\right\}. \tag{7}$$

Here $n_0(t')$, $n_{\mathrm{e}}(t')$ are the density of neutral atoms and free electrons, respectively. The absorption and dispersion effects of the medium on high harmonics are represented by δ_{h} and β_{h}. $D(r,z',t')$ is the single-atom induced dipole moment, which was calculated by the QRS model.

If we consider radiation in the gas medium is uniform (plane wave) in the transverse direction, the 3D propagation equations can be reduced to one-dimensional (1D) ones, in which the component of Laplacian in the r direction is ignored [50]. The resulting equations for fundamental laser and high-harmonic fields are

$$-\frac{2i\omega}{c}\frac{\partial\tilde{E}_1\left(z',\omega\right)}{\partial z'}=\tilde{G}\left(z',\omega\right), \tag{8}$$

$$-\frac{2i\omega}{c}\frac{\partial\tilde{E}_{\mathrm{h}}\left(z',\omega\right)}{\partial z'}=-\omega^2\mu_0\tilde{P}\left(z',\omega\right). \tag{9}$$

Once equations (5) and (6) or (8) and (9) are numerically solved, high harmonics at the exit face of gas medium are obtained. They will be called near-field harmonics.

2.3. Far-field high harmonics

In the experiment, near-field harmonics diverge as they propagate in the vacuum for a long distance before being measured by the spectrometer. The harmonics at the detector plane are called far-field harmonics. They can be calculated from near-field through a Hankel transformation [36, 51],

$$E_{\mathrm{h}}^{\mathrm{f}}\left(r_{\mathrm{f}},z_{\mathrm{f}},\omega\right)=-ik\exp\left[ik\left(\sqrt{z_{\mathrm{f}}^2+r_{\mathrm{f}}^2}-z_{\mathrm{f}}\right)\right]\times\int\frac{\tilde{E}_{\mathrm{h}}\left(r,z',\omega\right)}{z_{\mathrm{f}}-z'}J_0\left(\frac{krr_{\mathrm{f}}}{z_{\mathrm{f}}-z'}\right)\exp\left[\frac{ik\left(r^2+r_{\mathrm{f}}^2\right)}{2\left(z_{\mathrm{f}}-z'\right)}\right]rdr. \tag{10}$$

Here the near-field position (with respect to laser focusing) is z', radial distance at the far-field plane is r_{f}, and the position of the far-field from the laser focus is z_{f}. The first term on the right-hand side is to eliminate the optical path difference caused by the different radial distance r_{f}. J_0 is the zero-order Bessel function, and $k=\omega/c$ is the wave vector.

2.4. Time-frequency analysis and synthesis of attosecond pulses

To discern emission features in time for frequency-resolved high harmonics, the technique of time-frequency analysis is applied for harmonic field $E_{\mathrm{h}}(t)$. Such analysis based on wavelet transform [52–54] is expressed as

$$A(t',\omega)=\int E_{\mathrm{h}}(t)\sqrt{\omega}W\left[\omega\left(t-t'\right)\right]dt. \tag{11}$$

We used the Morlet wavelet [55]:

$$W(x) = \left(\frac{1}{\sqrt{a_0}}\right) e^{ix}\, e^{-x^2/2a_0^2}, \tag{12}$$

here a_0 is a constant. For better temporal resolution, it was chosen as 12 and 16 for 800 and 2000 nm lasers, respectively.

For the generation of attosecond pulse, spectral filtering is applied for a selected range of harmonics (ω_1–ω_2). Since near-field high harmonics are generated in a quite focused area, we calculate the total near-field attosecond pulse. Its intensity is obtained by integrating over radial distance r as [36]

$$I_{\text{near}}\left(t'\right) = \int_0^r 2\pi \left| \int_{\omega_1}^{\omega_2} E_{\text{h}}(r,\omega) e^{i\omega t'} d\omega \right|^2 r dr. \tag{13}$$

High harmonics in the far field may be divergent, thus the intensity of a far-field attosecond pulse is calculated as [36]

$$I_{\text{far}}\left(t'\right) = \int_{r_1}^{r_2} 2\pi \left| \int_{\omega_1}^{\omega_2} E_{\text{h}}^{\text{f}}\left(r_{\text{f}},\omega\right) e^{i\omega t'} d\omega \right|^2 r_{\text{f}} dr_{\text{f}}. \tag{14}$$

Here r_1–r_2 specifies a spatial range in the far field (or a range of divergence angles).

3. Results and discussion

3.1. Attosecond pulses driven by ideal beams with IR and MIR lasers

In this work, we choose two laser wavelengths, 800 nm and 2000 nm in the IR and MIR, respectively. The full-width-at-half-maximum durations for both lasers are taken to be 10 optical cycles. They are considered as long-duration lasers in terms of the number of laser periods. The CEP is 0. The peak intensity for the 800 nm (2000 nm) laser is set at 1.8×10^{14} W cm^{-2} (1.15×10^{14} W cm^{-2}) such that the ionization probability at the peak of laser pulse calculated by the ADK ionization model [56] is 3.61% (0.57%). These numbers are consistent with the 'critical' ionization value for Ar atom. A short 2 mm long gas cell is employed in the modeling. The density of Ar gas in the interaction volume is taken to be uniformly distributed since the size of gas cell is much larger than the beam waists used.

We first simulate the HHG by solving 1D propagation equations, i.e. the driving laser and harmonic field are both modeled as plane-wave beams. The calculated harmonic spectra by varying gas pressure are shown in figures 1(a) and (b). One can see the high-order harmonics are extended into the SXRs if the 2000 nm laser is used. At the lowest gas pressure of 5 Torr, both 800- and 2000 nm lasers produce fast highly oscillating harmonics over the whole spectral range. By increasing gas pressure, the harmonic yields are increased but the oscillations in the spectra become damped. We use the harmonics in the cutoff region (indicated by dashed lines) to synthesize attosecond pulses, e.g. 45–65 eV (in the XUV) and 135–185 eV (in the SXRs) for short and long wavelengths, respectively. The resulting attosecond pulses versus gas pressure are plotted in figures 1(c) and (d). Note that the lower pressure results have been multiplied by some factors for easy comparison. For the 800 nm laser, with the increase of gas pressure, the number of emitted attosecond pulses is gradually decreased until an IAP appears at 100 Torr, where the maximum peak intensity is achieved as well. When gas pressure is increased to 150 Torr, in the time domain it shows a two-peak attosecond pulse. This structure maintains with further increase of gas pressure while the peak intensity is gradually decreased. For the 2000 nm laser, the number of pulse trains is quickly reduced when gas pressure is increased from 5 Torr to 50 Torr. Above 50 Torr, the IAP always occurs for any gas pressures. At the optimal pressure of 150 Torr, the IAP reaches its maximum intensity. Clearly the generation of IAP at short and long wavelengths on pressure are quite different.

3.2. Mechanism of transient phase-matching gating

To reveal the mechanism of IAPs generated with IR and MIR lasers, we next analyze the harmonic emission at optimal gas pressures. In figures 2(a) and (b), we show the time-frequency analysis of harmonic fields at the exit plane of the gas medium for the two wavelengths. One can see that the emission burst of cutoff harmonics constantly appears at −0.5 o.c., which is labeled by 'E'. We show the electric field of the driving laser in a moving frame with the speed of light at propagation distances $z = 0$, 1, and 2 mm, i.e. the entrance, the middle point, and the exit plane of gas cell, respectively, in figures 2(c) and (d). Near −1 o.c., which is indicated by the label 'B', the overlap of electric fields for the three propagation distances z is the best. After about 2/3 o.c., the electron ionized at this moment has returned to and has recombined with the atomic ion to emit high harmonics at 'E', as labeled in figures 2(a) and (b). They can be added coherently during propagation in the medium. For other optical cycles, the electric waveforms at different z's do not

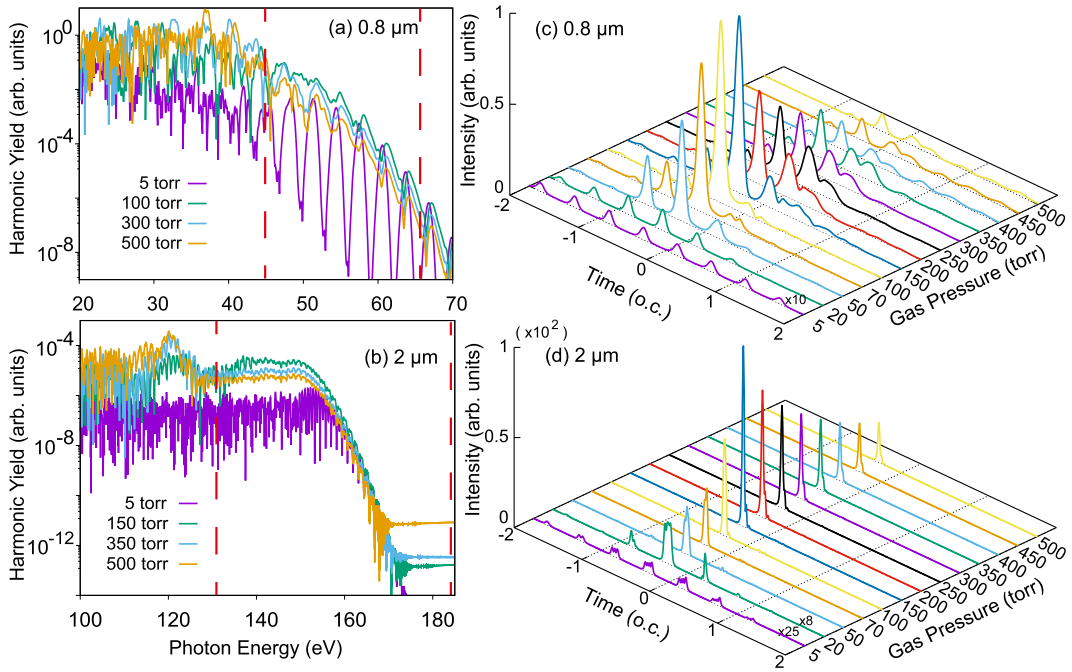

Figure 1. Simulated gas pressure dependence of macroscopic high-harmonic spectra with 0.8 μm (a) and 2 μm (b) lasers. The harmonic yield is plotted in logarithmic scale. The fundamental laser and high-harmonic fields are both assumed to be 1D ideal beams. Attosecond pulses obtained by synthesizing cutoff harmonics from 45–65 eV (c) and from 135–185 eV (d) (indicated by dashed lines in (a) and (b), respectively). o.c. stands for the optical cycle of the laser. See text for simulation parameters.

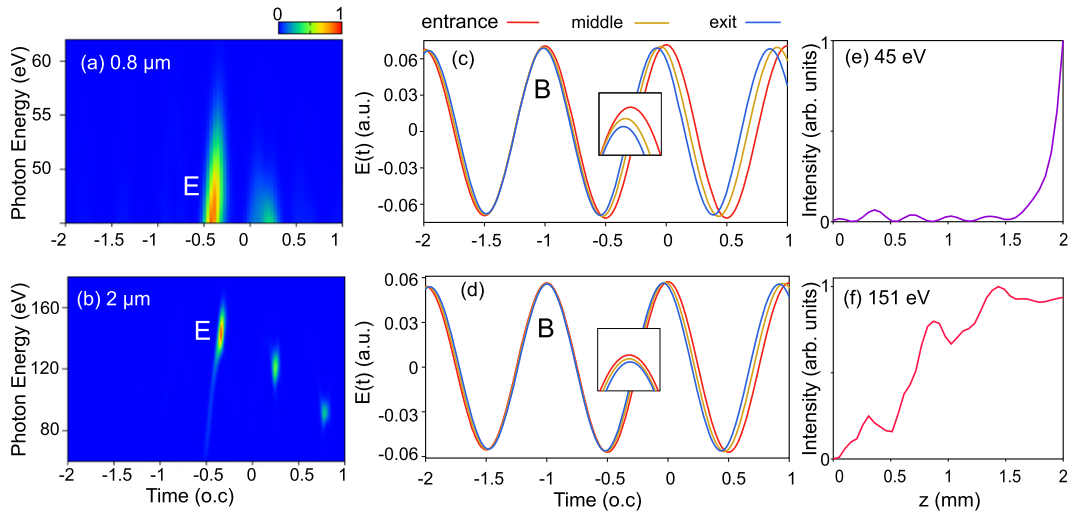

Figure 2. (a) and (b) Time-frequency analysis of high harmonics at the exit plane of gas cell. (c) and (d) Waveform of fundamental electric field at different propagation positions: entrance at $z = 0$ mm, middle at $z = 1$ mm, and exit at $z = 2$ mm. 'B' is used to label the time where the electron is released, which is related to harmonic emission labeled by 'E' in (a) and (b). (e) and (f) Buildup of harmonic field in the gas medium for selected photon energy of 45 eV (or 151 eV). The simulations with 800 nm laser at optimal pressure of 100 Torr are shown in the first row, while the second row is for 2000 nm laser at pressure of 150 Torr.

phase match well for both wavelengths, thus the harmonic fields cannot grow. Since phase matching can be achieved only in a short time interval of a long pulse, the method for IAPs thus generated is called transient phase-matching gating.

We next compare with the difference between the two driving wavelengths. The evolution of the electric field in the gas medium is governed by the dispersion of the neutral atoms and plasma, and absorption by the free electrons, thus the field is depleted along the propagation distance. Since the ionization level of the 800 nm laser is higher than that of the 2000 nm laser, its depletion and temporal shift of electric field with z is much more significant, which is evidenced by the enlarged views at -1 o.c. and also by the mismatch of electric waveforms at other optical cycles, see figures 2(c) and (d). By looking at the enlarged views more

Table 1. Coherence lengths of 45 eV and 151 eV harmonics generated by 0.8 μm and 2 μm lasers, respectively. The coherence length is calculated by equation (15) through the phase mismatch Δk_q.

0.8 μm	100 Torr					150 Torr				
Time (o.c.)	−2	−1.5	−1	−0.5	0	−2	−1.5	−1	−0.5	0
Δt (as)	58	19	−13	−52	97	71	32	−6	−39	84
ΔI (I_0)[a]	−0.26	−0.39	−0.44	−0.57	−0.66	−0.31	−0.40	−0.44	−0.53	−0.68
L_{col} (mm)	0.85	1.91	22.8	1.45	0.68	0.70	1.28	3.44	2.11	0.81
2 μm	150 Torr					200 Torr				
Time (o.c.)	−2	−1.5	−1	−0.5	0	−2	−1.5	−1	−0.5	0
Δt (as)	211	122	8	−114	−252	277	154	16	−130	−301
ΔI (I_0)	0.09	0.18	0.25	0.31	0.34	−0.13	−0.24	−0.31	−0.39	−0.431
L_{col} (mm)	0.13	0.22	2.82	0.24	0.11	0.10	0.17	1.69	0.2	0.09

carefully, for 800 nm laser, the electric fields from entrance to middle point are changed more rapidly compared to those from middle point to exit plane, and for 2000 nm laser, the change of electric fields from entrance to exit is much smoother, thus explaining the buildup of harmonic field with z for the two selected cutoff energies of 45 and 151 eV, as plotted in figures 2(e) and (f). The cutoff harmonics generated by short wavelength are efficiently built up only in the second half of gas medium while those generated by long wavelength can be accumulated over the whole range of the medium.

The behavior of the growth of cutoff harmonics with different laser wavelengths can be quantitatively interpreted by calculating the coherence length of harmonics. Such analysis can also explain why transient phase-matching gating is sensitive to gas pressure for the 800 nm laser, but not so for the 2000 nm laser. Since the driving laser is reshaped during propagation in the medium, the coherence length can be calculated from the phase mismatch as [57, 58]

$$L_{\mathrm{col}} = \frac{\pi}{\Delta k_{\mathrm{q}}} \approx \frac{\pi \Delta z}{\left[(q-1)\omega_0 \Delta t - \alpha_i \Delta I\right]}. \tag{15}$$

Here q is the harmonic order, ω_0 is the frequency of the driving laser and Δt (ΔI) is the shift of peak electric field in time (intensity) for a propagation distance Δz. The coefficient α_i is used for calculating the induced-dipole phase accumulated by the electron in the laser field, which scales as λ_{L}^3. For cutoff harmonics, $\alpha_{\mathrm{cutoff}} \approx 13.7 \times 10^{-14}$ rad cm^2 W^{-1} at 800 nm [59]. To evaluate the coherence length, Δz is chosen according to the propagation distance for effective harmonic growth. As shown in figures 2(e) and (f), for cutoff harmonics, Δz can be defined between $z = 1$ and 2 mm at 800 nm, while it is between $z = 0$ and 2 mm at 2000 nm. For optimal pressures, Δt (ΔI) around −2, −1.5, −1, −0.5, and 0 o.c. derived from electric fields in figures 2(c) and (d) are listed in table 1, and similar data for other pressures are also given. For the 0.8 μm laser, at 100 Torr, the calculated coherence length for the 45 eV harmonic is 22.8 mm at −1 o.c., which is much larger than that obtained at other optical cycles. Thus, the harmonics emitted around −0.5 o.c. can be best phase-matched in the second half of gas cell. At 150 Torr, the coherence lengths at −1 and −0.5 o.c. are 3.44 and 2.11 mm, respectively, and they are very close. Thus, the harmonics caused by the ionization of electrons at these moments can be added up coherently, leading to double-peak temporal structure as seen in figure 1(c). This explains that transient phase-matching gating at 800 nm is easily missed by varying the gas pressure. The situation is different for 2000 nm laser. At optimal pressure of 150 Torr, the maximum coherence length for the 151 eV harmonic is 2.82 mm, occurring at −1 o.c., which is larger than the whole length of gas cell. The coherence lengths obtained at other optical cycles are about one order of magnitude smaller. The similar big difference between coherence lengths at −1 o.c. and at other moments can be identified at 200 Torr as well. Therefore, only harmonic field due to the ionized electrons at −1 o.c. can be substantially built up in the gas medium, leading to an efficient transient phase-matching gating, which is not readily affected by gas pressure.

Note that our proposed mechanism for IAP is different from the time-gated phase matching presented by Hernández-García *et al* [60] for a loose focusing geometry of Bessel beam. The reshaping of laser pulse during propagation in the gas medium is critical to identify the IAP mechanism reported here. In their technique, the absorption and group velocity matching plays a key role for generating IAP using long wavelength multi-cycle pulses. Their method works for both IR and MIR driving lasers and is not dependent much on gas pressure for long-duration pulses.

3.3. Attosecond pulses generated by Gaussian beams

The transient phase-matching gating has been demonstrated for an ideal MIR beam. Does it work for a real Gaussian beam when phase mismatches due to the geometric phase (or generally called Gouy phase) and

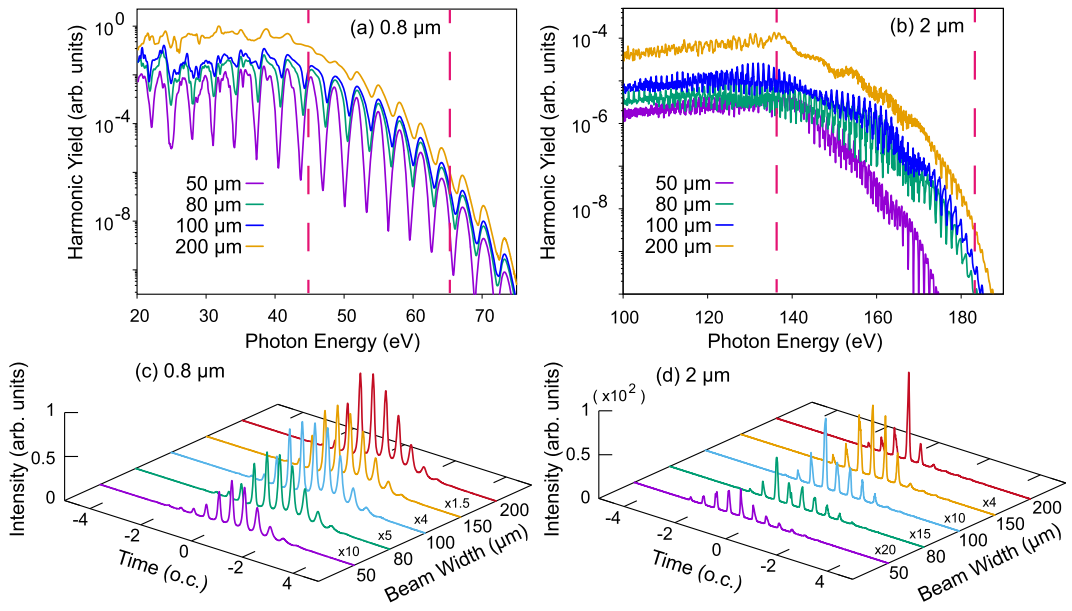

Figure 3. (a) and (b) Total macroscopic high harmonic spectra collected at the near field for Gaussian beams with varying beam waists. (c) and (d) Attosecond pulses by spectrally filtering high harmonics from 45–65 eV in (a) and from 135–185 eV in (b). Gas pressure is fixed at 150 Torr. Note that the harmonic yield is given on logarithmic scale.

Table 2. Pulse energies of fundamental laser (W_f) and attosecond pulses (W_h), and conversion efficiencies (η) of high harmonics for 0.8- and 2 μm lasers, respectively. The interested high harmonics of 45–65 eV (or 135–185 eV), are generated by 0.8 μm (or 2 μm) laser at the optimal pressure of 100 Torr (or 150 Torr) with different beam waists, which are used to synthesize the attosecond pulses.

	800 nm			2000 nm		
w_0 (μm)	W_f (mJ)	η	W_h (nJ)	W_f (mJ)	η	W_h (pJ)
50	0.22	6.8×10^{-7}	0.15	0.38	5.1×10^{-9}	1.94
80	0.57	1.0×10^{-6}	0.57	0.96	3.4×10^{-9}	3.26
100	0.89	1.3×10^{-6}	1.16	1.51	4.7×10^{-9}	7.10
150	2.00	2.5×10^{-6}	5.00	3.39	6.5×10^{-9}	22.04
200	3.57	3.0×10^{-6}	10.71	6.03	9.1×10^{-9}	54.87

induced-dipole phase are also considered? To answer this question, we solve the 3D propagation equations of the fundamental laser and high-harmonic fields. In the simulations, a 2 mm long Ar gas cell is used and its center is located at the laser focus. Gas pressure is fixed at 150 Torr. Peak intensity at the laser focus is 2.0×10^{14} W cm^{-2} (1.35×10^{14} W cm^{-2}) for the 0.8 μm (2 μm) laser, which is higher than that for the ideal beam, to ensure that 'critical' ionization occurs in a large off-axis volume. The calculated macroscopic HHG spectra at different beam waists are shown in figures 3(a) and (b). The spectra are obtained by integrating over the whole exit face of the gas medium. The spectral filter is applied so cutoff harmonics (indicated by dashed lines) are synthesized to produce attosecond pulses. The resulted intensity profiles of attosecond pulses are shown in figures 3(c) and (d). Some factors are multiplied at small beam waists for easy comparison. The pulse energies of attosecond pulses are listed in table 2, which are derived from the conversion efficiencies of HHG. And the conversion efficiency is gradually increased with the increase of beam waist except for two beam waists at 2 μm. One expects that with the increase of beam waist, the laser focusing effect becomes weaker and results seen in the ideal beam should appear. This is not the case for the 800 nm laser. The number of APTs is not changed at all when the beam waist w_0 is increased from 50 to 200 μm, see figure 3(c). For the 2000 nm laser, the pulse energy of attosecond pulse at the same beam waist is about two order of magnitude smaller than that for 800 nm laser in table 2, however, the amount of SXR attosecond emission bursts is gradually reduced with the increase of beam waist. At $w_0 = 200$ μm, one strong attosecond pulse appears with a few weak subpeaks. This indicates that transient phase-matching gating still taking place for a loosely focused Gaussian beam with MIR wavelength. Note that the corresponding pulse energy is about 55 pJ from table 2, which is comparable to or better than that of SXR harmonics observed in laboratories. For example, in Li *et al* [28], for the 53 as pulse covering photon

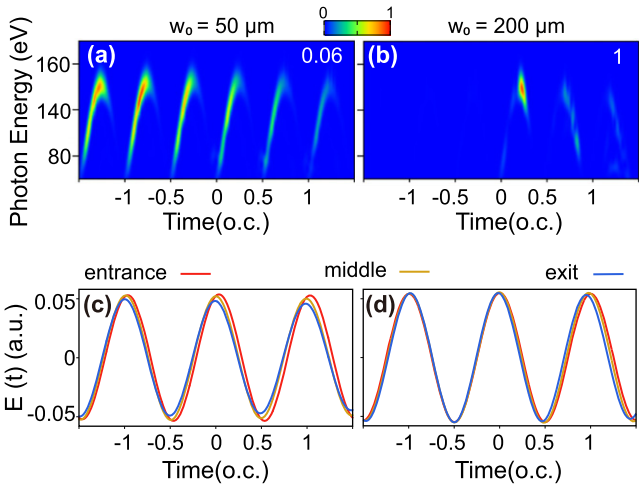

Figure 4. (a) and (b) Time-frequency analysis of high harmonics at $r = 0.35w_0$ of the exit plane, where w_0 is the beam waist. (c) and (d) At the same radial distance, the driving electric fields are shown at the entrance of $z = -1$ mm, the middle of $z = 0$ mm, and the exit of $z = 1$ mm. The first column is for $w_0 = 50$ μm, the second one is for $w_0 = 200$ μm. Laser wavelength and gas pressure are fixed at 2 μm and 150 Torr, respectively.

energies from 100 to 300 eV, the flux is estimated to be about 5×10^6 photons per laser shot, and its pulse energy is close to 100 pJ. In Johnson *et al* [32], the pulse energy of measured water-window harmonics in Neon is 2 pJ. Cousin *et al* [27] reported that the SXR high harmonics from 284 to 350 eV with flux of 5.6×10^6 photons/s at repetition rate of 1 kHz, which results in a much lower pulse energy of about 0.3 pJ. From these comparisons, our predicted SXR attosecond pulses can be easily measurable experimentally.

To demonstrate the transient phase-matching gating further, we show the time-frequency analysis of harmonic emissions driven by the 2000 nm laser for a tightly focused beam (50 μm) with that for a loosely focused beam (200 μm) in figures 4(a) and (b). These figures again show that the number of harmonic emission bursts is greatly reduced by increasing the beam waist. The electric fields at the entrance, middle, and exit plane of gas cell are also plotted for two beam waists in figures 4(c) and (d). Only for the beam waist of 200 μm the overlap of electric fields at different z is the same as that for an ideal beam.

3.4. Generation of isolated attosecond pulses in the far field with MIR lasers

Can the subpeaks generated by the 200 μm MIR beam in figure 3(d) be separated from the major peak for the attosecond pulses? To resolve this problem, we look at the spatial distributions of attosecond pulses at the near and far fields in figures 5(a) and (b), respectively. Considerable harmonic bursts are mostly located at different radial distances in the near field because of Gaussian distribution of the laser intensity along r. Due to reshaping of laser pulse during propagation, harmonic bursts in different optical cycles can be projected onto the far field with different divergence angles, see figure 5(b). Using a spatial filter (within 1 mrad) to select attosecond pulses labeled as 'E_i' ($i = 1$–4) individually, the intensity profiles are plotted in figure 5(c). The major peak labeled as 'E_1' is seen separated from other subpeaks and presents itself as an IAP with duration of 420 as. The subpeaks ('E_2', 'E_3', and 'E_4') show up at different time intervals in the form of either an APT or an IAP with much weak intensities. Since the half-angle of a Gaussian beam is given by $\theta = \lambda_L/\pi w_0$, its divergence is about 3 mrad for 2 μm laser with beam waist w_0 of 200 μm. Thus the generated IAP at 'E_1' can be spatially separated from the driving laser. Note that the pulse energy of 2 μm laser is about 6 mJ, the repetition rate can reach to about 170 kHz when the average power exceeding 1 kW [61–66]. How to separate the driving laser and generated high harmonics with high-repetition-rate lasers has been addressed recently [67–69]. Thus our proposed scheme is especially favorable for the generation of IAP with high-repetition-rate laser.

The IAP above is obtained at a fixed CEP of a 2 μm laser. To check whether CEP needs to be stabilized, we use the same generation and collection parameters as those in figure 5 but change the CEP from zero to π. The intensity profiles of the attosecond pulses are plotted in figure 6. A clean IAP can be generated when the CEP either equals to 0, π or 0.2 π, while double peaks are presented at other CEPs. This means that our gating method requires stable CEP of a long-duration laser, but stabilization error within about 0.2 π is acceptable.

The IAP in figure 5(c) is produced at the optimal pressure of 150 Torr. What about other pressures if the geometry of Gaussian beam is loose focusing? At the beam waist of 200 μm, we calculate the similar near-field attosecond pulses to those in figure 3(d) by increasing gas pressure from 5 to 250 Torr as shown

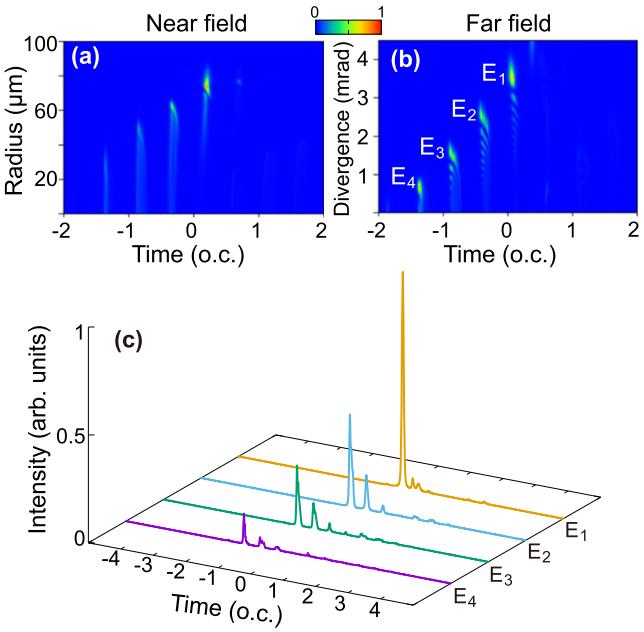

Figure 5. Spatial distribution of attosecond pulses generated with 2 μm laser at the near field (a) and at the far field (b). (c) Intensity profiles of attosecond pulses collected within 1 mrad at different positions labeled as 'E_i' in (b), where $i = 1$–4. Waist of the Gaussian beam is 200 μm and gas pressure is 150 Torr.

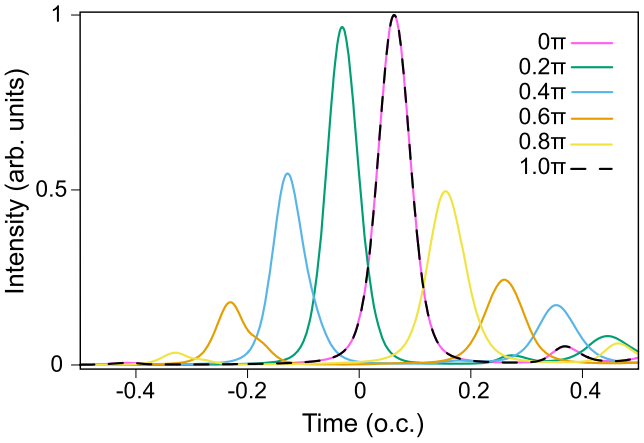

Figure 6. Intensity profiles of attosecond pulses, which are the same as that at 'E_1' in figure 5(c) except that the CEP of the driving laser is varied.

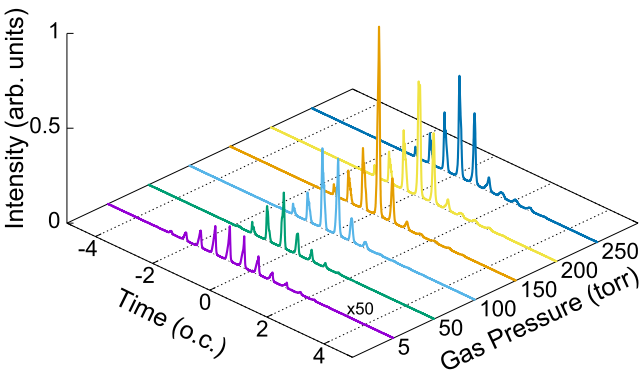

Figure 7. Gas-pressure dependent attosecond pulses in the near field obtained with cutoff harmonics by a 2 μm laser when beam waist $w_0 = 200$ μm.

in figure 7. The temporal structures appearing at the optimal pressure can also be found at other pressures once the gas pressure is larger than 50 Torr. Therefore, IAP is also expected to be generated in the far field but with decreased peak intensity if gas pressure is not matched with the optimal one.

4. Conclusions

In summary, we have proposed a transient phase-matching gating method to generate IAP in the SXR region with multi-cycle, MIR laser pulses. First, employing a 1D ideal beam under the 'critical' ionization condition for 800- and 2000 nm laser pulses, we have investigated the pressure dependence of attosecond pulses synthesized with cutoff harmonics in the XUV and the SXR regions, respectively. The 'critical' ionization is met when phase mismatch caused by the free electrons is compensated by that from atomic dispersion. Transient phase-matching gating has been found to work better for long-wavelength laser pulses. We have demonstrated this result by evaluating the evolution of the electric fields during the propagation in the medium, and by calculating the coherence length of HHG at different time intervals. The reshaping of laser pulse along propagation distance is a key ingredient of the gating method. We have further examined the transient phase-matching gating method for 3D Gaussian beams. We have found that the gating method predicts a great reduction of the number of cycles of APTs for a loosely focused MIR beam. With the help of laser-induced wavefront rotation, the far-field harmonics are divergent and SXR IAPs are produced by spatial filtering. We have also verified that such IAP generation is quite robust, which depends weakly on the CEP of the driving MIR laser and gas pressure.

With the development of laser technology, high-power, high-repetition-rate MIR lasers are becoming available in the laboratories. Our gating method may provide an opportunity to combine these technologies to efficiently produce SXR IAPs for wide applications. In this work, we have demonstrated the generation of IAP with gating method by using an Gaussian beam. Other spatial beams, such as non-divergent Bessel beam, flat-top beam, and super-Gaussian beam [70], and other HHG generation setups, for instance, in a hollow waveguide [71], may use the present method for generating SXR IAPs in the future.

Acknowledgments

This work was supported by the National Natural Science Foundation of China (11774175, 91950102, and 11834004); CDL was supported by Biosciences Division, Office of Basic Energy Sciences, Office of Science, US Department of Energy (DE-FG02-86ER13491). We thank Professor Yuxi Fu at Xi'an Institute of Optics and Precision Mechanics, Chinese Academy of Sciences for useful discussions on pulse energies of attosecond pulses.

Data availability statement

All data that support the findings of this study are included within the article (and any supplementary files).

ORCID iDs

C D Lin https://orcid.org/0000-0003-4847-8938
Cheng Jin https://orcid.org/0000-0001-8445-2378

References

[1] Krausz F and Ivanov M 2009 *Rev. Mod. Phys.* **81** 163–234
[2] Peng L-Y, Jiang W-C, Geng J-W, Xiong W-H and Gong Q 2015 *Phys. Rep.* **575** 1–71
[3] Han S, Li J, Zhu Z, Chew A, Larsen E W, Wu Y, Pang S S and Chang Z 2020 *Adv. At. Mol. Opt. Phys.* **69** 1–65
[4] Cousin S L, Silva F, Teichmann S, Hemmer M, Buades B and Biegert J 2014 *Opt. Lett.* **39** 5383–6
[5] Popmintchev T *et al* 2012 *Science* **336** 1287–91
[6] Popmintchev D *et al* 2015 *Science* **350** 1225–31
[7] Schafer K J, Yang B, DiMauro L F and Kulander K C 1993 *Phys. Rev. Lett.* **70** 1599–602
[8] Corkum P B 1993 *Phys. Rev. Lett.* **71** 1994–7
[9] Paul P M, Toma E S, Breger P, Mullot G, Augé F, Balcou P, Muller H G and Agostini P 2001 *Science* **292** 1689–92
[10] Hentschel M *et al* 2001 *Nature* **414** 509–13
[11] Goulielmakis E *et al* 2008 *Science* **320** 1614–7
[12] Ferrari F, Calegari F, Lucchini M, Vozzi C, Stagira S, Sansone G and Nisoli M 2010 *Nat. Photon.* **4** 875–9
[13] Sansone G *et al* 2006 *Science* **314** 443–6
[14] Mashiko H, Gilbertson S, Li C, Khan S D, Shakya M M, Moon E and Chang Z 2008 *Phys. Rev. Lett.* **100** 103906

[15] Zhao K, Zhang Q, Chini M, Wu Y, Wang X and Chang Z 2012 *Opt. Lett.* **37** 3891–3
[16] Vincenti H and Quéré F 2012 *Phys. Rev. Lett.* **108** 113904
[17] Greening D *et al* 2020 *Opt. Express* **28** 23329–37
[18] Takahashi E J, Lan P, Mücke O D, Nabekawa Y and Midorikawa K 2013 *Nat. Commun.* **4** 2691
[19] Xue B, Tamaru Y, Fu Y, Yuan H, Lan P, Mücke O D, Suda A, Midorikawa K and Takahashi E J 2020 *Sci. Adv.* **6** eaay2802
[20] He L, Yuan G, Wang K, Hua W, Yu C and Jin C 2019 *Photon. Res.* **7** 1407–15
[21] Schötz J *et al* 2020 *Phys. Rev.* X **10** 041011
[22] Takahashi E J, Kanai T, Ishikawa K L, Nabekawa Y and Midorikawa K 2008 *Phys. Rev. Lett.* **101** 253901
[23] Hong K-H, Lai C-J, Siqueira J P, Krogen P, Moses J, Chang C-L, Stein G J, Zapata L E and Kärtner F X 2014 *Opt. Lett.* **39** 3145–8
[24] Sanchez D, Hemmer M, Baudisch M, Cousin S L, Zawilski K, Schunemann P, Chalus O, Simon-Boisson C and Biegert J 2016 *Optica* **3** 147–50
[25] Chen M-C *et al* 2014 *Proc. Natl Acad. Sci.* **111** E2361–7
[26] Zhao X, Wang S J, Yu W W, Wei H, Wei C, Wang B, Chen J and Lin C D 2020 *Phys. Rev. Appl.* **13** 034043
[27] Cousin S L, Di Palo N, Buades B, Teichmann S M, Reduzzi M, Devetta M, Kheifets A, Sansone G and Biegert J 2017 *Phys. Rev.* X **7** 041030
[28] Li J *et al* 2017 *Nat. Commun.* **8** 186
[29] Gaumnitz T, Jain A, Pertot Y, Huppert M, Jordan I, Ardana-Lamas F and Wörner H J 2017 *Opt. Express* **25** 27506
[30] Silva F, Teichmann S M, Cousin S L, Hemmer M and Biegert J 2015 *Nat. Commun.* **6** 6611
[31] Teichmann S M, Silva F, Cousin S L, Hemmer M and Biegert J 2016 *Nat. Commun.* **7** 11493
[32] Johnson A S *et al* 2018 *Sci. Adv.* **4** eaar3761
[33] Fu Y, Nishimura K, Shao R, Suda A, Midorikawa K, Lan P and Takahashi E J 2020 *Commun. Phys.* **3** 92
[34] Tate J, Auguste T, Muller H G, Salières P, Agostini P and DiMauro L F 2007 *Phys. Rev. Lett.* **98** 013901
[35] Shiner A D *et al* 2009 *Phys. Rev. Lett.* **103** 073902
[36] Jin C, Le A T and Lin C D 2011 *Phys. Rev.* A **83** 023411
[37] Colosimo P *et al* 2008 *Nat. Phys.* **4** 386–9
[38] Popmintchev T, Chen M-C, Bahabad A, Gerrity M, Sidorenko P, Cohen O, Christov I P, Murnane M M and Kapteyn H C 2009 *Proc. Natl Acad. Sci.* **106** 10516–21
[39] Rundquist A, Durfee C G, Chang Z, Herne C, Backus S, Murnane M M and Kapteyn H C 1998 *Science* **280** 1412–5
[40] Durfee C G, Rundquist A R, Backus S, Herne C, Murnane M M and Kapteyn H C 1999 *Phys. Rev. Lett.* **83** 2187–90
[41] Nefedova V E *et al* 2018 *Phys. Rev.* A **98** 033414
[42] Morishita T, Le A T, Chen Z and Lin C D 2008 *Phys. Rev. Lett.* **100** 013903
[43] Lin C D, Le A-T, Jin C and Wei H 2018 *J. Phys. B: At. Mol. Opt. Phys.* **51** 104001
[44] Le A T, Lucchese R, Tonzani S, Morishita T and Lin C D 2009 *Phys. Rev.* A **80** 013401
[45] Lewenstein M, Balcou P, Ivanov M Y, L'Huillier A and Corkum P B 1994 *Phys. Rev.* A **49** 2117–32
[46] Le A T, Morishita T and Lin C D 2008 *Phys. Rev.* A **78** 023814
[47] Zhao S-F, Wang Y, Wang G and Zhou X-X 2014 *Opt. Commun.* **328** 30–6
[48] Tosa V, Kim H, Kim I and Nam C H 2005 *Phys. Rev.* A **71** 063807
[49] Gaarde M B, Tate J L and Schafer K J 2008 *J. Phys. B: At. Mol. Opt. Phys.* **41** 132001
[50] Priori E *et al* 2000 *Phys. Rev.* A **61** 063801
[51] Tosa V, Kim K T and Nam C H 2009 *Phys. Rev.* A **79** 043828
[52] Kim J H, Lee D G, Shin H J and Nam C H 2001 *Phys. Rev.* A **63** 063403
[53] Yakovlev V S and Scrinzi A 2003 *Phys. Rev. Lett.* **91** 153901
[54] Gaarde M 2001 *Opt. Express* **8** 529–36
[55] Tong X M and Chu S I 2000 *Phys. Rev.* A **61** 021802
[56] Tong X M and Lin C D 2005 *J. Phys. B: At. Mol. Opt. Phys.* **38** 2593–600
[57] Jin C and Lin C D 2016 *Phys. Rev.* A **94** 043804
[58] Jin C, Chen M-C, Sun H-W and Lin C D 2018 *Opt. Lett.* **43** 4433–6
[59] Gaarde M B and Schafer K J 2002 *Phys. Rev.* A **65** 031406
[60] Hernández-García C, Popmintchev T, Murnane M M, Kapteyn H C, Plaja L, Becker A and Jaron-Becker A 2017 *Opt. Express* **25** 11855–66
[61] Russbueldt P, Mans T, Weitenberg J, Hoffmann H D and Poprawe R 2010 *Opt. Lett.* **35** 4169–71
[62] Krebs M, Hädrich S, Demmler S, Rothhardt J, Zaïr A, Chipperfield L, Limpert J and Tünnermann A 2013 *Nat. Photon.* **7** 555–9
[63] Negel J-P, Loescher A, Voss A, Bauer D, Sutter D, Killi A, Ahmed M A and Graf T 2015 *Opt. Express* **23** 21064–77
[64] Hädrich S, Jan Rothhardt J, Krebs M, Demmler S, Klenke A, Tünnermann A and Limpert J 2016 *J. Phys. B: At. Mol. Opt. Phys.* **49** 172002
[65] Müller M, Kienel M, Klenke A, Gottschall T, Shestaev E, Plötner M, Limpert J and Tünnermann A 2016 *Opt. Lett.* **41** 3439–42
[66] Saule T *et al* 2019 *Nat. Commun.* **10** 458
[67] Gaumnitz T, Jain A and Wörner H J 2018 *Opt. Lett.* **43** 4506–9
[68] Klas R, Kirsche A, Tschernajew M, Rothhardt J and Limpert J 2018 *Opt. Express* **26** 19318–27
[69] Jin C, Tang X, Li B, Wang K and Lin C D 2020 *Phys. Rev. Appl.* **14** 014057
[70] Strelkov V V, Mével E and Constant E 2008 *New J. Phys.* **10** 083040
[71] Jin C, Stein G J, Hong K H and Lin C D 2015 *Phys. Rev. Lett.* **115** 043901